Lasers in Surgery and Medicine 51:920–932 (2019)

# Optical Access to Arteriovenous Cerebral Microcirculation Through a Transparent Cranial Implant

**Nami Davoodzadeh,[1] Mildred S. Cano-Velázquez,[2] David L. Halaney,[1] Carrie R. Jonak,[3] Devin K. Binder,[3] and Guillermo Aguilar[1]***

[1]*Department of Mechanical Engineering, University of California, Bourns Hall A342 900 University Ave., Riverside, California, 92521*

[2]*Instituto de Investigaciones en Materiales, Universidad Nacional Autónoma de México, Circuito Exterior S/N, Ciudad Universitaria, Coyoacán, Mexico City, 04510, Mexico*

[3]*Division of Biomedical Sciences, School of Medicine, University of California, 1126 Webber Hall 900 University Ave., Riverside, California, 92521*

**Background and Objective:** Microcirculation plays a critical role in physiologic processes and several disease states. Laser speckle imaging (LSI) is a full-field, real-time imaging technique capable of mapping microvessel networks and providing relative flow velocity within the vessels. In this study, we demonstrate that LSI combine with multispectral reflectance imaging (MSRI), which allows for distinction between veins and arteries in the vascular flow maps produced by LSI. We apply this combined technique to mouse cerebral vascular network in vivo, comparing imaging through the skull, to the dura mater and brain directly through a craniectomy, and through a transparent cranial "Window to the Brain" (WttB) implant.

**Study Design/Materials and Methods:** The WttB implant used in this study is made of a nanocrystalline Yttria-Stabilized-Zirconia ceramic. MSRI was conducted using white-light illumination and filtering the reflected light for 560, 570, 580, 590, 600, and 610 nm. LSI was conducted using an 810 nm continuous wave near-infrared laser with incident power of 100 mW, and the reflected speckle pattern was captured by a complementary metal-oxide-semiconductor (CMOS) camera.

**Results:** Seven vessel branches were analyzed and comparison was made between imaging through the skull, craniectomy, and WttB implant. Through the skull, MSRI did not detect any vessels, and LSI could not image microvessels. Imaging through the WttB implant, MSRI was able to identify veins versus arteries, and LSI was able to image microvessels with only slightly higher signal-to-noise ratio and lower sharpness than imaging the brain through a craniectomy.

**Conclusions:** This study demonstrates the ability to perform MSRI-LSI across a transparent cranial implant, to allow for cerebral vascular networks to be mapped, including microvessels. These images contain additional information such as vein-artery separation and relative blood flow velocities, information which is of value scientifically and medically. The WttB implant provides substantial improvements over imaging through the murine cranial bone, where microvessels are not visible and MSRI cannot be performed. Lasers Surg. Med. © 2019 Wiley Periodicals, Inc.

**Key words:** transparent nanocrystalline yttria-stabilized-zirconia; brain imaging; arteriovenous cerebral microcirculation; laser speckle imaging; multispectral reflectance imaging

## INTRODUCTION

Microcirculation, usually defined as small arteries (<150 μm in diameter), arterioles, capillaries, and venules [1,2], plays a critical role in the physiological processes of tissue oxygenation and nutrient exchange within the brain [3,4]. In recent years, the recognition that microcirculation is also involved in a number of pathophysiologic processes has further increased interest in its study [3]. Microcirculation can be measured in several ways, including (but not limited to) morphological imaging methods to measure vessel density, perfusion rate, vessel diameter, and dynamic measurements of microcirculatory blood flow velocity and blood cell concentration [3], as well as functional imaging methods to provide information on blood oxygenation, changes in metabolism, regional chemical composition, and so on [5].

Various imaging modalities have been developed, which are capable of measuring blood flow. Although they have

Conflict of Interest Disclosures: All authors have completed and submitted the ICMJE Form for Disclosure of Potential Conflicts of Interest and none were reported. Contract grant sponsor: National Science Foundation; Contract grant number: NSF-PIRE #1545852; Contract grant sponsor: National Council of Science and Technology of Mexico (CONACYT); Contract grant number: 741249.

*Correspondene to: Guillermo Aguilar, Department of Mechanical Engineering, University of California, Bourns Hall A342 900 University Ave., Riverside, CA 92521.
E-mail: gaguilar@engr.ucr.edu

Accepted 1 June 2019
Published online 24 June 2019 in Wiley Online Library (wileyonlinelibrary.com).
DOI 10.1002/lsm.23127

resulted in a number of discoveries, there are notable drawbacks which should be considered in developing a scalable and real-time method for routine long-term brain microcirculation monitoring. Magnetic resonance imaging (MRI) and blood-oxygenation-level-dependent MRI [6,7] are very expensive and large imaging tools [8]. Dynamic contrast enhanced computed tomography (CT) and micro-CT [9,10] have a lower resolution than MRI and rely on ionizing radiation making it infeasible for monitoring [8]. Digital subtraction angiography (DSA) is an invasive and time-consuming method [11,12]. Indocyanine green video angiography requires injection of dyes and cannot provide continuous assessment of vessel perfusion [13,14]. Optical coherence tomography (OCT) [15], photoacoustic imaging (PAM) [16], and fluorescence microscopy approaches like confocal microscopy or the two-photon variant [17] are based on laser scanning limiting the temporal resolution and field of view [18], although recent technical improvements in OCT and PAM have been reported, which provide sufficient temporal resolution for epileptic seizure monitoring [19–21]. Ultrasound (US) and micro-US [22] imaging depth is larger than light-based approaches, however, the resolution is poorer [23]. Fast full-field laser Doppler perfusion imaging (ffLDPI) [17] cannot simultaneously provide microvascular structural and functional information because of lacking adequate spatiotemporal resolution [24].

Laser speckle imaging (LSI), on the other hand, is a full-field, real-time, noninvasive, and non-contact imaging method with is sensitive to both the speed and morphological changes of the scattering particles, and is capable of mapping relative velocity in flow fields such as capillary blood flow [17]. LSI produces blood flow maps in a fraction of a second without the need for scanning, by utilizing the spatial statistics of time-integrated speckle, making it a true real-time technique [17]. Like LSI, ffLDPI can provide full field information in a short time and may be regarded as its main competing technique, but LSI has the advantage of being relatively simple and cheap since it does not require a high-speed imaging array, and can also be coupled with other imaging modalities [17].

In addition to information on vessel geometry and flow characteristics, distinction between arteries and veins is of great clinical importance. The ability to independently render veins and arteries on blood perfusion maps has a variety of potential applications in the head, neck, lungs, heart, abdomen, and lower extremities, and most critically in the cerebrovascular system including brain arteriovenous malformation and dural arteriovenous fistulas [25], cerebral hemorrhage, stroke, and aneurysm [26].

Multispectral reflectance imaging (MSRI) is a simple and low-cost method capable of distinguishing between veins and arteries based on differences in the optical absorption of oxyhemoglobin and deoxyhemoglobin. This method has been developed in visible and near-infrared (NIR) wavelength range [27–34]. This method involves a white light source, optical filters, and a camera, and can easily be coupled with LSI [26,31,35]. Indeed, a single instrument combining laser speckle flowmetry and MSRI has been demonstrated in a rodent thinned skull model [28] for simultaneous relative cerebral blood flow and hemoglobin oxygen saturation changes during ischemia [31,36,37] and functional activation [38]. A thinned skull preparation was necessary due to the high scattering and absorption of the skull in the visible and NIR range, which limits the accessibility of MSRI wavelengths for detecting hemoglobin oxygenation information [39,40]. When MSRI has been applied through the intact skull, only skull regions and not individual microvessels are visible [40,41]. Likewise, in our own prior studies we have found that imaging through intact skull with LSI limits the size of vessels that can be detected, and precludes imaging of the microcirculation [42,43]. Moreover, the absorption and reflectance features of the inhomogeneous cranial bone overlap with those of brain tissue, and the skull also has its own vessels. Together, these factors decrease the accuracy and reliability of the data.

Studies in the literature have addressed this optical barrier with various approaches including imaging the brain directly with an opened skull [35], thinned, and polished skull preparations [44,45], temporary optical clearing of the skull using optical clearing agents [46–48], and implanting glass or poly-di-methyl-siloxane (PDMS) windows [49,50]. Glass and PDMS windows are powerful research techniques, but are not appropriate for human application as permanent cranial implants for patients. Like skull thinning and polishing techniques, glass-based windows compromise protection for the brain due to the extremely low fracture toughness of typical glasses (KIC = 0.7–0.9 MPa $m^{1/2}$) [51], which increases the potential for catastrophic failure by fracture, while the effect of skull optical clearing agents for long-term use on human skull is unknown [42]. A number of biomedical considerations including biocompatibility, mechanical strength, and ageing should be examined in order to create an optical window for eventual clinical application [42]. Conventional cranial prosthesis including titanium, alumina, and acrylic [52] have not provided the requisite combination of transparency and toughness required for clinically-viable transparent cranial implants. To address this challenge, our group has previously introduced a transparent nanocrystalline yttria-stabilized-zirconia cranial implant material, which possesses the mechanical strength and biocompatibility that are prerequisites for a clinically-viable permanent cranial implant for patients [41,42,53–56]. We refer to this in the literature as the "Window to the Brain" (WttB) implant. Yttria-stabilized zirconia (YSZ) represents an attractive alternative, due to its relatively high toughness (KIC ~8 MPa m1/2) [57], as well as its proven biocompatibility in dental and orthopedic applications [58]. Additional benefits of this material over imaging through skull include its stable optical behavior and lack of optical absorption by water (Fig. 1c). We envision this implant as a potential future optical access to the brain allowing for real-time monitoring of arteriovenous cerebral blood flow (Fig. 1).

In this present study, we performed cerebral arteriovenous microcirculation imaging by combining MSRI and LSI techniques. This method was applied in a mouse model, first through the closed skull, then to the dura mater and brain directly after a craniectomy was performed to remove a piece of skull, and finally through the WttB implant after the

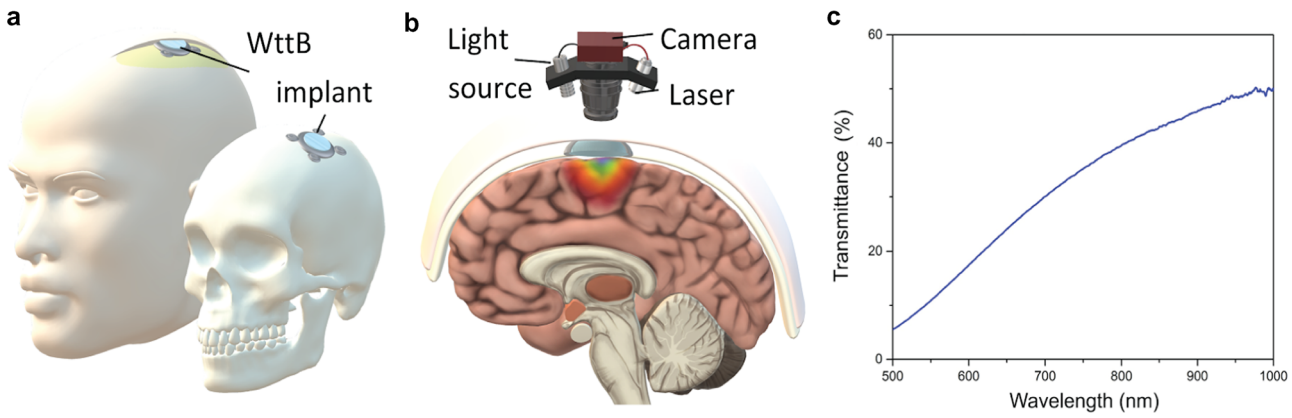


Fig. 1. (**a**, **b**) Illustration of the Window to the Brain concept as envisioned for future human application, to allow for real-time monitoring of arteriovenous cerebral blood flow. (**c**) Transmittance spectra of Window to the Brain implant.

implant was placed within the craniectomy on the dura mater. The imaging obtained through the WttB implant and through the skull were compared to the imaging obtained through the open skull, which served as a reference. The goal of this study was to assess the improvement in brain imaging with MSRI-LSI when captured through the WttB implant versus imaging through the skull.

## MATERIALS AND METHODS

### Transparent Stabilized-Zirconia Cranial Implant

Transparent nanocrystalline 8 mol% $YO_{1.5}$ yttria-stabilized zirconia (nc-YSZ) implant sample used in this study was densified into a transparent bulk ceramic from precursor YSZ nanopowder (Tosoh USA, Inc., Grove City, OH). The densification method utilized for this purpose consists of a current-activated pressure-assisted densification procedure developed by Garay et al. [59] and described extensively. The thickness of the resulting densified YSZ disc was reduced from 1 mm to ~300 μm by polishing with 30 μm diamond slurry on an automatic polisher (Pace Technologies, Tucson, AZ). The sample was then polished with successively finer diamond and silica slurries ranging from 6 to 0.2 μm. A rectangular section of approximately $2.1 \times 2.2$ mm was cut from the polished YSZ disc using a diamond lapping saw (WEIYI DTQ-5, Qingdao, China), followed by sonication in acetone and thorough rinsing in water. Optical transmittance spectra for the polished implant is shown in Figure 1c.

### Animals

All experimental procedures and humane care of mice were conducted in compliance with the University of California, Riverside Institutional Animal Care and Use Committee approval. The $N = 1$ 12-week-old C57Bl/6 male mouse (Jackson Laboratory, Bar Harbor, ME) used in this study was housed under a 12-hour light and 12-hour dark cycle with ad libitum access to food and water.

### Surgical Procedures

The mouse was implanted with a WttB implant as described previously [43]. Briefly, the mouse was anesthetized with isoflurane inhalation (0.2–0.5%), and given

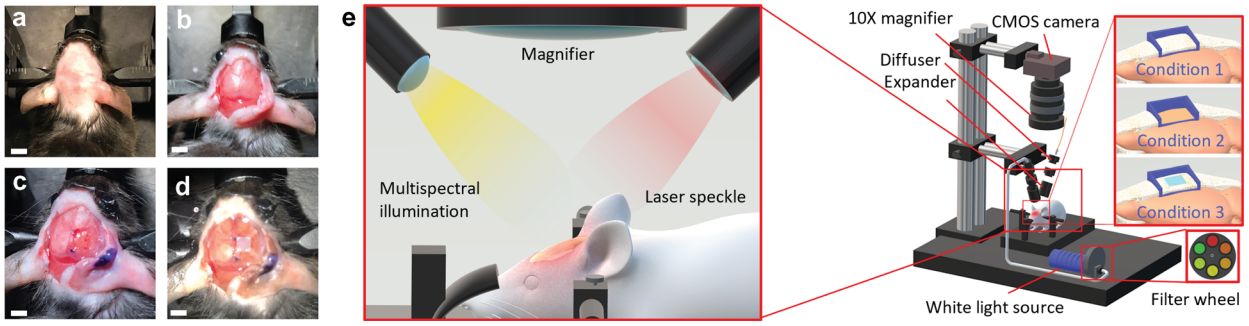


Fig. 2. (**a**–**d**) Surgical preparations including shaved scalp (scale bars = 2 mm) (**a**), intact skull (i.e., condition 1) (**b**), open skull (i.e., condition 2) (**c**), and WttB implant (i.e., condition 3) (**d**). (**e**) Schematic of the experimental imaging setup including laser speckle imaging (LSI) and multispectral reflectance imaging (MSRI). The inset shows a schematic of the imaging fields of view on murine cranium, with the blue tetragonals representing the imaging field.

ketamine and xylazine (K/X) (80/10 mg/kg, i.p.). Additional anesthetic was administered as necessary. Hair was removed from the scalp using clippers (Fig. 2a). The mouse was then secured into a stereotaxic frame to immobilize the head for surgery. Ophthalmic ointment was placed over the eyes, and the surgical site was sterilized with alternating application of betadine and 70% EtOH (three times). The implant was also sterilized in 70% EtOH. A sagittal incision was made to the left of the midline, and the scalp retracted to expose the skull (Fig. 2b). Periosteum was removed from the skull, and a craniectomy was performed with a surgical drill and carbide burr to remove a square section of skull over the right parietal lobe, with dimensions slightly larger than the implant (Fig. 2c). The WttB implant was placed within the craniectomy directly on the intact dura mater, and dental cement was applied to each of the four corners of the implant to prevent displacement (Fig. 2d). Dental cement was cured with UV light exposure for 20 seconds. Imaging was conducted with the scalp open, before craniectomy with the skull closed (condition 1), immediately after craniectomy with the skull open (condition 2), and after the WttB implantation (condition 3).

### MSRI and LSI

MSRI was performed by optically filtering a white-light source (MI-150; Dolan-Jenner, Boxborough, MA). Optical bandpass filters mounted on a fast-change filter wheel (FW103H; Thorlabs, Newton, NJ) were used to isolate different spectral components and provided a six-wavelength (560, 570, 580, 590, 600, and 610 nm) multispectral dataset, as shown in Figure 2e. For LSI, an 810 nm continuous wave NIR laser (DL808-7W0-O; CrystaLaser, Reno, NV) was used to illuminate the region of interest with incident power of 100 mW at a 45° incidence. While most LSI studies use visible wavelengths for illumination, we chose 810 nm to reduce reflectance and increase transmittance through the WttB implant (see Fig. 1c). The 810 nm laser intensity was homogenized using a diffuser (ED1-C20-MD; Thorlabs) and was expanded using a pair of negative-positive lenses (KPC043, −25 mm EFL and KPX094, 100 mm EFL; Newport, Irvine, CA). Multispectral incoherent light and diffused laser light were sequentially shown onto the closed skull (i.e., condition 1), onto the dura mater and cortex after craniectomy (i.e., condition 2) and through the WttB implant (i.e., condition 3). The reflected light from the illuminated region was captured by a 12-bit complementary metal-oxide-semiconductor (CMOS) camera (DCC1545M; Thorlabs), which was focused at the cortical surface using a ×10 zoom microscope (MLH-10X, 152.4 mm WD; Computar, Torrance, CA). For each imaging condition, a sequence of six multispectral images and 100 laser speckle images were captured. Laser speckle images were acquired at exposure times of 6 ms (per our previous report on optimized LSI exposure time [42]) at a speed of 14 frames per second. The aperture and magnification of the zoom microscope were carefully chosen to ensure that the speckle size at the image plane was approximate to the area of a single pixel in the CMOS chip [60–62]. A schematic of the imaging system is shown in Figure 2e. In image processing, each camera frame was registered to one another to ensure appropriate spatial alignment over the MSRI and LSI images. In MSRI, normalizing each individual wavelength to its corresponding white reference (WS-1; Ocean Optics, Oxford, UK) image compensated for variations in the illumination. The white reference images were captured through the WttB implant in condition 3.

### Vein-Artery Separation Using MSRI

The MSRI approach relies on the distinctive absorption spectra of oxy- and deoxyhemoglobin (HbO2 and HbR). The hemoglobin in blood is the most significant absorber in the brain at visible and NIR wavelengths. HbR and HbO2 have different absorption spectra, and thus based on the Beer-Lambert law [63], measurements with different wavelengths of light can produce images that are preferentially sensitive to difference in the concentration of HbO2 and HbR. At isobestic points, the HbR and HbO2 optical extinction coefficient are similar (568 and 587 nm). At 560, 600, and 610 nm, areas with higher level of deoxyhemoglobin C (e.g., the veins) leads to more optical extinction and thus makes the corresponding area darker (i.e., lower intensity values in the images), and therefore we can provide artery-vein separation. In this case, we assume that scattering in the brain does not change significantly during the experiment. To separate the vein and arteries in MSRI images, the vasculature branches were detected and mapped manually for seven branches in regular white-light images (Fig. 3a). Each vasculature branch was labeled by a number. To obtain the mean intensity of a branch, 10 samples of intensity ($4 \times 4$ pixels) were extracted and averaged from each branch and called vessel branch intensity. The sample intensities of each branch were evenly distributed along the midline of the main vessel of the branch (Fig. 3a). The samples locations were kept constant for each vasculature branch over the multispectral images. Then, normalized extinction was obtained over the wavelengths by calculating the difference in intensities of the white reference and the vessel branch, normalized by white reference intensity following Equation (1),

$$\text{Normalized extinction} = \frac{I_{n,\lambda} - I_{R,\lambda}}{I_{R,\lambda}} \tag{1}$$

where $I_{n,\lambda}$ is vessel branch number $n$, intensity at $\lambda$ wavelength, and $I_{R,\lambda}$ is the mean value of the white reference intensity at $\lambda$ wavelength.

### Rebuilding Arteriovenous Cerebral Blood Flowmetry Map Based on MSRI-LSI

*Step* 1: Constructing a blood flow map using laser speckle temporal contrast analysis (LSTCA)

The contrast-resolved LSI images were constructed in the same manner as our prior study [42], based on the temporal statistical analysis of laser speckle, which has been proven to preserve spatial resolution [61]. Experimental results have indicated that the temporal speckle contrast analysis could expressively suppress the effect of the static laser

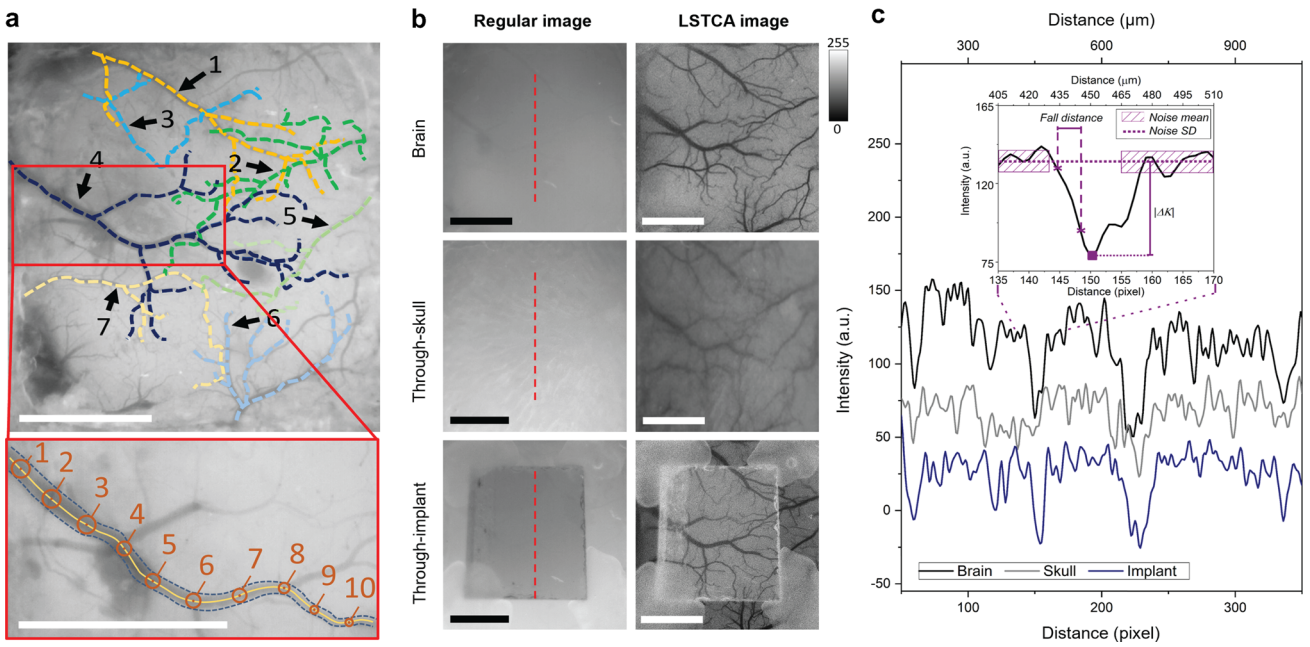


Fig. 3. (**a**) Vessels branches of 1–7 indicated by different colors on a regular white-light image of the brain image through the open skull (condition 2). The inset shows an example of evenly distributed intensity samples along the midline of the main vessel of the branch 4, which were used to calculate the vessel branch intensity. (**b**) Regular white-light images and laser speckle imaging (LSI) images (scale bars = 1 mm). (**c**) Contrast intensity profiles of lines across the images (shown as a dashed line in panel (**a**). The inset in (**c**) shows how LSI noise parameters, $|\Delta K|$ and fall distances are determined from the line profiles.

speckle pattern formed by the stationary superficial reflection and scattering tissue on the visualization of blood flow [60–62,64,65]. Suppressing this effect makes temporal contrast analysis an ideal method for imaging cerebral blood flow through mouse skull and the transparent WttB implant. The temporal contrast, $K_t$, of each image pixel in the time sequence was calculated using Equation (2) [60],

$$K_t(x,y) = \frac{\sigma_{(x,y)}}{\langle I_{(x,y)} \rangle} = \sqrt{\frac{1}{(N-1)}\left\{\sum_{n=1}^{N} [I_{(x,y)}(n) - \langle I_{(x,y)} \rangle]^2)\right\}} / \langle I_{(x,y)} \rangle \quad (2)$$

where $I_{x,y}(n)$ is the intensity at pixel $(x,y)$ in the nth image, $N$ is the number of images acquired, and $\langle I_{x,y} \rangle$ is the mean value of intensity at pixel $(x,y)$ over the $N$ images.

*Step* 2: Arteriovenous vasculature network

The vasculature network was extracted from the LSI image according to the difference in flow velocity between the vasculature and tissue. A Hessian-based filtering algorithm was then used to enhance contrast and connectivity in the image of the vasculature [66–68]. In this step, vessels are detected using the eigenvalues of the image [67], and detection is sensitive to vessels in any orientation. Vessel detection was performed over multiple vessel scales (from ~20 to 400 μm in diameter), and the maximum filter response for each pixel was used. The resulting image was thresholded to produce a binary mask of the vasculature. The arteriovenous information obtained by MSRI was then registered on the vasculature network obtained by LSI, and veins and arteries were labeled on the vasculature network LSI images.

*Step* 3: Weighting the arteriovenous vasculature network by the blood flow map

Finally, the resulted arteriovenous vasculature network was weighted by the calculated LSTCA relative blood flow information.

## Quantitative Analysis of the LSI Resolution and Contrast

We assessed the quality of the speckle contrast images in terms of signal to noise ratio (SNR) and vessel sharpness. To quantify signal to noise ratio for each imaging condition, the contrast intensity profile along a vertical line (across the blood vessels) was considered (Fig. 3b). The profile lines were chosen based on the open-skull images such that four vessels were intersected. The same spatial location (i.e., same vessels) were analyzed in the through-skull and through-implant conditions as well. When imaging through skull, one of the four vessels was

not visible and was omitted from the analysis of that condition. Figure 3c shows an example of the contrast intensity profile for the brain with open skull, through-skull, and through-implant. Equation (3) shows how SNR values were calculated for each exposure time and time point,

$$\mathrm{SNR} = \Delta K / \sigma K_n \tag{3}$$

where $\Delta K$ is the depth of the vessel peak from the baseline (mean noise) and $\sigma K_n$ is the standard deviation of the noise. A visual example of $\Delta K$ and $\sigma K_n$ are shown in Figure (3). The SNR values were averaged over the profile vessels and standard errors were calculated. Sensitivity, which is considered as the ratio of the mean SNR to the mean SNR of the reference, was calculated using Equation (4).

$$\text{Sensitivity} = \frac{\mathrm{SNR}_{\text{imaging condition } n}}{\mathrm{SNR}_{\text{imaging condition 2}}} \tag{4}$$

As an indicator of resolution, we compared the sharpness of the vessel edges in images by calculating the fall distance (the number of pixels) of the edge of the vessel to go from 10% to 90% of $\Delta K$ value [69]. A shorter fall distance corresponds to greater sharpness. The same sampled contrast intensity profiles were considered for the fall distance calculation. Figure 3c shows an example trace and 10–90% fall distance measurement. To compare the blood vessel images through-skull and through-implant, the fall distances were determined and averaged over the profile vessels and the standard errors were calculated.

## RESULTS

### MSRI Images of the Brain: Comparison of Through-Skull and Through-Implant Images

The mapped vasculature branches and vein-artery separated network from open-skull imaging (i.e., condition 2) are shown in Figure 4a and b, respectively. Figure 4d shows the spectral behavior of the branches. The dashed line in Figure 4d shows the mean optical extinction of all seven branches. Overall, optical extinction is relatively high for wavelengths of 560–580 nm. A drastic decrease in optical extinction happens at wavelengths of 590, 600, and 610 nm. Notably, the vessel branches 1 and 4 show a different trend compared to branches 2, 3, 5, 6, and 7. These two groups were labeled in red and blue and the mean (solid lines) and standard deviation (colored shadow) of each group were separately calculated and shown. The blue group including branches 1 and 4 resulted in higher optical extinction at 560 nm. At wavelengths of 570 and 580 nm, red group showed the extremum values. Optical extinction values of red group have a higher decrease than the blue group at 590 nm and show lower optical extinction values at wavelengths of 590, 600, and 610 nm than the blue group. Comparing the relation between red and blue groups to the reported configuration of oxyhemoglobin and deoxyhemoglobin chromophores, optical extinction coefficients in the wavelength range of 560–610 nm [70] illustrates the existence of a higher concentration of oxyhemoglobin and relatively lower concentration of deoxyhemoglobin in the red group (vessel branches 2, 3, 5, 6, and 7) than the blue group (vessel branches 1 and 4).

A regular white-light image of the closed mouse skull (i.e., condition 1) is shown in Figure 5a. The MSRI images captured through the cranial bone of the mouse do not show the vasculature network. Consequently, we were not

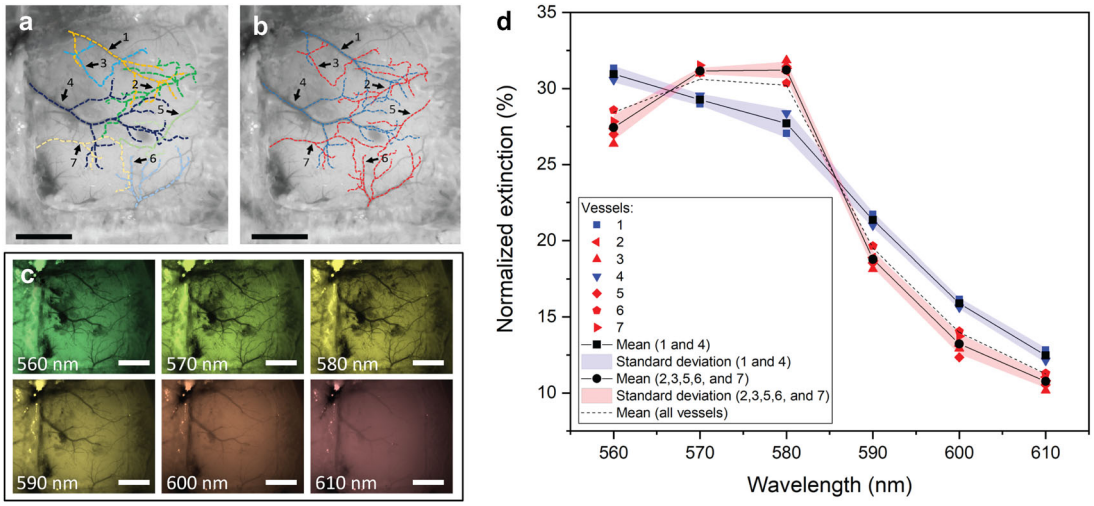


Fig. 4. Cerebral arteries-veins separation using multispectral reflectance imaging (MSRI), in open skull imaging (i.e., condition 2). (**a**) Labeling the vasculature branches on a regular white-light image. The images were converted to gray color map to make the colored vasculature branches clear. (**b**) The separated veins (blue) and arteries (red) (scale bars = 1 mm). (**c**) Optical images of the brain illuminated by various wavelengths. (**d**) Relative optical absorption values plotted for each branch.

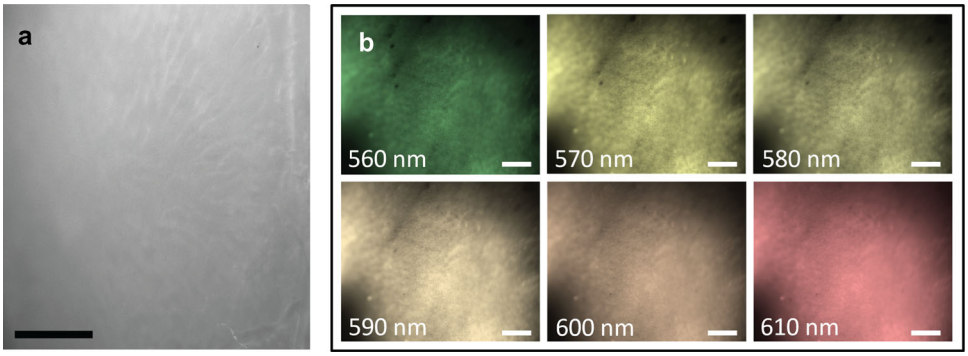


Fig. 5. The multispectral reflectance imaging (MSRI) through closed skull (i.e., condition 1). (**a**) Regular white-light image of the skull. The image was converted to gray color map to increase contrast. (**b**) Optical images of the mouse skull illuminated by various wavelengths. As seen, the vasculature map is not evident when imaged through skull (scale bars = 1 mm).

able to identify the vessels branches and their intensities over the multispectral images in Figure 5b.

Figure 6a shows mapped vasculature branches on a regular white-light image through the WttB implant (i.e., condition 3). Multispectral images as shown in Figure 6c resulted in a notable lower contrast compared with the references images (Fig. 4c). The spectral behavior of the branches is plotted in Figure 6d. The dashed line indicating the overall mean optical extinction for all seven branches shows a general decrease in the relative optical extinction compared with imaging the brain directly (Fig. 4c), which is due to the reflected light from the WttB implant surface overcoming the vessels optical extinction. Similar to the direct brain images (imaging condition 2), the mean optical extinction (dashed line) is relatively high for wavelengths of 560–580 nm, followed by a decrease at wavelengths of 590, 600, and 610 nm. Although there is a lower deviation between the optical extinction values, the separate trend of the vessel branches 1 and 4 compared with branches 2, 3, 5, 6, and 7 is still noticeable. Accordingly, these two groups were labeled in red and blue and the mean and standard deviation of each group were separately calculated and shown in Figure 6d. The analysis of the images obtained through WttB implant (imaging condition 3), shows a similar conclusion to the reference data (imaging condition 2). Although the relative optical extinction values have a notably higher deviation (which affects the

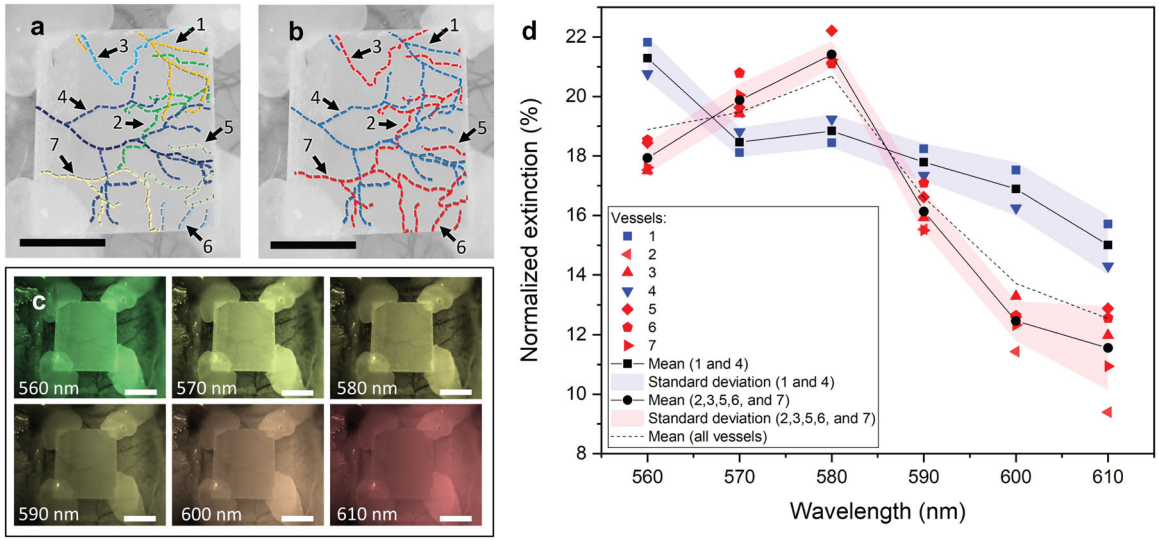


Fig. 6. Cerebral arteries-veins separation using multispectral reflectance imaging (MSRI) through the Window to the Brain (WttB) implant (imaging condition 3). (**a**) Labeling the vasculature branches on a regular white-light image of the implantation region (condition 3). (**b**) The separated veins (blue) and arteries (red). (**c**) Optical images of the brain illuminated by various wavelengths. (**d**) Normalized mean intensity values plotted for each branch.

accuracy of the analysis) compared with imaging the brain directly, the vein-artery separation is indeed doable through the WttB implant.

### Comparison of the Improved LSI Image Quality: Through-Implant Versus Through-Skull

Figure 3b shows regular white-light images and LSI temporal contrast images of brain, through-skull, and through-implant. It should also be noted that after the surgery, blood flow is expected to be altered in response to the invasive craniectomy surgery (e.g., due to potential reactive hyperemia [71] (increased blood flow), changes in respiration, etc.). We previously reported the optimal exposure time for LSI imaging at each time point, so that we could compare the images of highest SNR that could be acquired of the brain, through-skull, and through-implant.

Line intensity profiles like the example shown in Figure 3c were analyzed for the brain, through-skull, and through-implant contrast images. To avoid selection bias, the location of these line profiles were chosen arbitrarily at the region of interest (ROI) mid-points, as depicted in the regular white-light image in Figure 3b. From these intensity profiles, peak intensity and noise were determined (as described in the Methods section and illustrated in the inset of Fig. 3c), and SNR ratio was calculated. Data for each imaging condition was averaged between the vessels and the mean SNR for each imaging condition is shown in Figure 7a. As expected, the brain contrast image shows the highest SNR (imaging condition 2). The through-implant contrast image (imaging condition 3) resulted in the higher SNR compared with the through-skull contrast image (imaging condition 1) by 17.59% (relatively).

Sensitivity was calculated and resulted in 96.82% for the through-implant image (imaging condition 3) and 86.1% for the through-skull image (imaging condition 1). Then, we compared the sharpness (i.e., fall distance) of the vessels in the images to determine if the images were becoming blurred and losing resolution through the WttB implant. The mean fall distance for each imaging condition is shown in Figure 7b. The through-implant contrast image (imaging condition 3) provided 5.7 μm lower fall distance (higher sharpness) when compared with the through-skull contrast image (imaging condition 1).

### Assessing Arteriovenous Blood Flow Through-Implant

Figure 8 demonstrates the process of arteriovenous cerebral microcirculation image generation and the images obtained through each step. First, an LSI image is acquired, which contains information on vessel structures and relative flow velocities. The LSI image is also thresholded to provide a contrasted vessel map as a reference vasculature network (step 1). Next, MSRI imaging allows for separating cerebral veins and arteries based on optical extinction spectra over the wavelengths 560–610 nm, and this arteriovenous information is overlaid on the vasculature network LSI image (step 2). Finally, the arteriovenous vasculature network image is weighted by the relative blood flow velocities obtained during the initial LSI imaging in step 1 (step 3).

## DISCUSSION

The WttB holds the transformative potential for facilitating diagnosis and treatment of a wide variety of brain pathologies and neurological disorders. We envision this implant enabling delivery to and/or acquisition of light from the brain, in real-time, without the need for repeated highly-invasive craniotomies. Such access may also create a new platform for understanding the brain.

In this study we assessed feasibility of MSRI-LSI imaging of the brain microcirculation through the WttB implant.

Other studies have investigated various methods of vein-artery separation, including velocity-based [72,73], optical attenuation-based methods other than MSRI [26], and structural-based separation [74]. Besides the

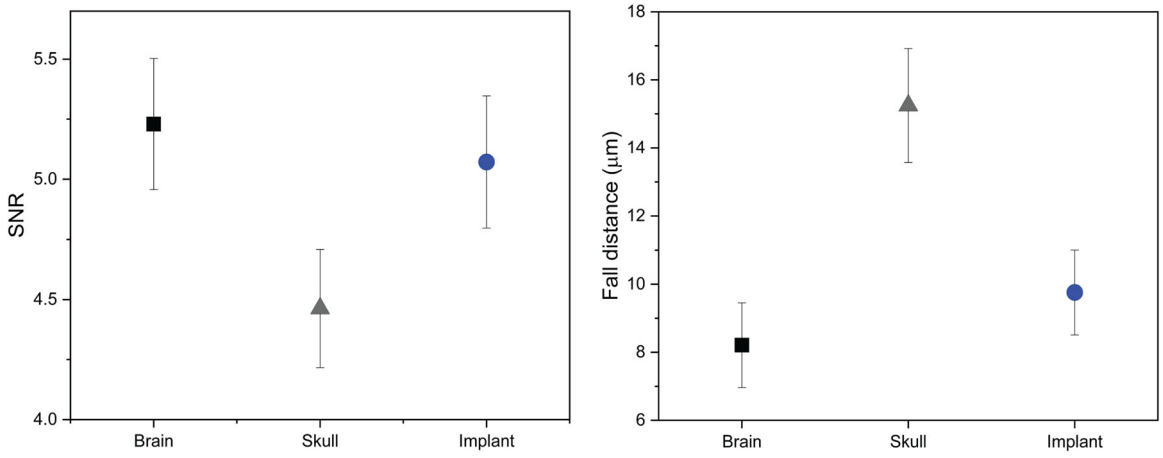


Fig. 7. (**a**) Mean signal to noise ratio (SNR) of contrast intensity and (**b**) mean fall distance of contrast intensity along arbitrary line profiles on the brain, skull, and Window to the Brain (WttB) implant.

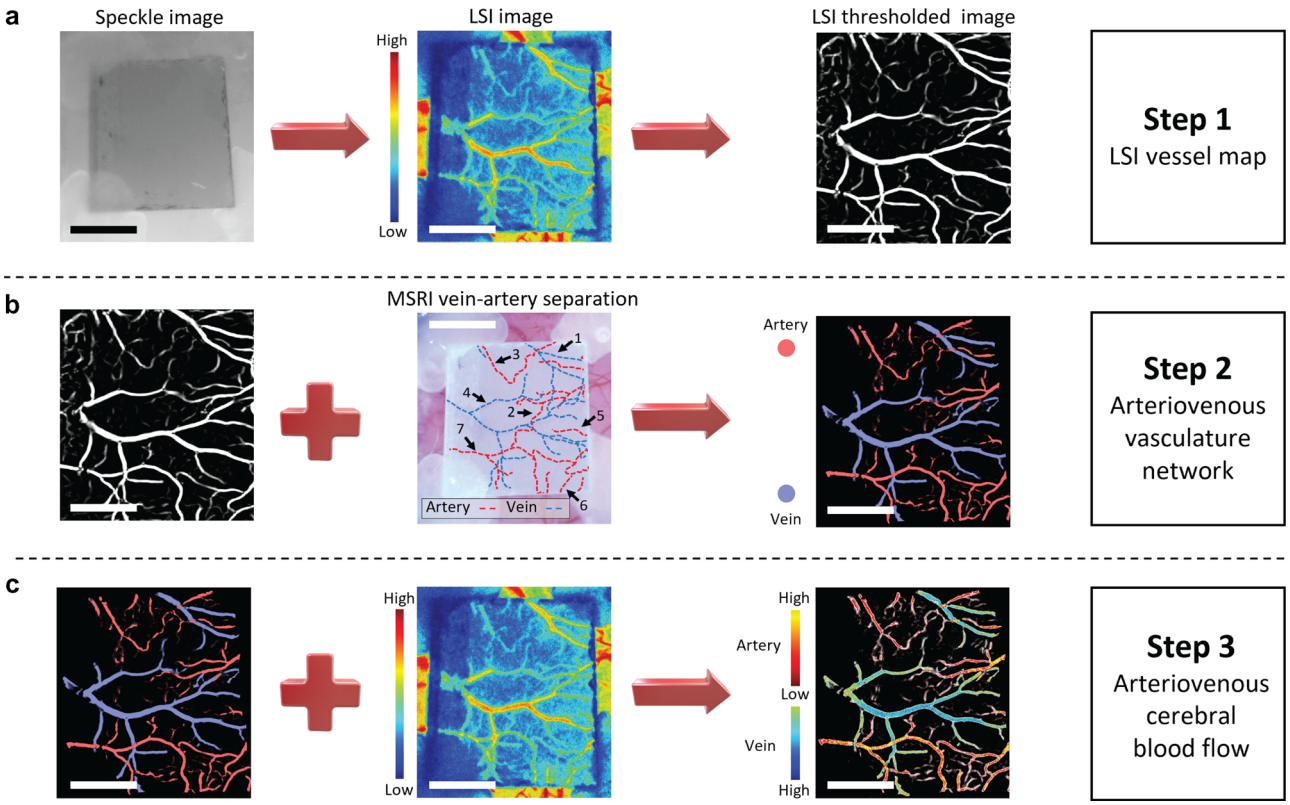


Fig. 8. The steps of constructing an arteriovenous microcirculation image. (**a**) Laser speckle imaging (LSI) image obtained by temporal analysis of laser speckle images. The LSI images were then processed to generate the LSI vessel map, where bright is the vasculature network and dark is the non-vascular region (step 1). (**b**) Arteriovenous information from multispectral reflectance imaging (MSRI) is registered onto LSI vasculature network obtained using LSI (step 2). (**c**) Arteriovenous vascular network is weighted by the blood flow map (LSI image) (step 3). Bar = 1 mm.

various proposed methods based on multi-wavelength imaging [75–79], like the MSRI approach we used in this present study, Miao et al. [80] distinguished arteries and veins by vascular anatomical features and optical intensity profiles in single-wavelength laser speckle contrast imaging (SW-LSCI) images, but arteries and veins may be misclassified because of similar absorption to the cerebral cortex. Feng et al. [81] proposed an automatic vein-artery separation method based on imaging the exposed cerebral cortex using SW-LSCI, however, the absorption and scattering of underlying parenchyma would also influence the accuracy of the vein-artery separation. Our method for accessing the intrinsic information of blood using MSRI with six wavelengths utilizes more complex instrumentation than many of these other reported methods of vein-artery separation [26,74,82]. Our reason for choosing the MSRI method over less complex vein-artery separation methods was that MSRI allows for functional imaging, which can be useful in our future functional brain imaging studies through the WttB implant. However, limitations exist for extracting componential information from intrinsic optical signals (IOSs). Optical properties of blood constituents other than hemoglobin (Hb), may absorb or scatter light, and these may alter the optical transmission of blood vessels, which can affect the measurement of hemoglobin [83].

The analysis of the MSRI images acquired through the open craniectomy (condition 2) clearly shows the different spectral behaviors of veins and arteries. For all vessels imaged, veins showed greater optical extinction in wavelengths of 560, 590, 600, and 610 nm, while arteries showed greater optical extinction at wavelengths of 570 and 580 nm. When the brain was imaged through skull (condition 1), only the main vessels were barely visible and analysis of MSRI for the microcirculation was not practical. On the other hand, the MSRI images obtained through the WttB implant (condition 3) resulted in a clear map of the vessels, although some of the microvessels were not visible. Comparing the vessel branches optical extinction shows similar results to the reference data (condition 2). Branches 1 and 4 were detected as vein with higher optical extinction at 560, 590, 600, 610 nm and branches 2, 3, 5, 6, and 7 resulting in higher

optical extinction at 570 and 580 nm were thus identified as arteries. This result demonstrates that WttB implant can allow for reliable vein-artery separation imaging. It is worthwhile to mention that the images captured through the WttB implant have lower contrast, which limits the accuracy of the measurements when compared with imaging the brain directly. Lower average of optical extinction values in images through the WttB implant (16.98%) compared with open skull images (22.33%) shows this poorer contrast. Consequently, this lower contrast resulted in lower accuracy of the measurement shown by higher SD of red and blue groups. Averaged SD of red and blues groups is relatively increased by 33% and 31%, respectively, compared with open skull images.

Temporal contrast imaging has become a useful tool for brain blood flow applications as the images it produces contain functional information (i.e., relative blood velocity) in addition to showing structure of the vessel networks. As we previously reported, exposure time of 6 ms gave the highest SNR for both skull and WttB implant and was used for comparing SNR and sharpness of vessels imaged beneath each. Unlike our previous study with compared two different spatial regions, here the comparison was made between three different imaging conditions. Thus, SNR and sharpness of vessels (fall distance) are evaluated for an identical target. Accordingly, we were able to compare the SNR values of through-implant and through-skull images to the reference image (open skull) to evaluate the sensitivity. This supplementary information to our previous study on SNR further demonstrates that the SNR of through-implant image is higher than that of through-skull imaging. Vessels imaged through the WttB implant have shorter fall distances, while vessels imaged through the skull have greater fall distances, indicating that vessels imaged through the implant have sharper borders compared to those imaged through the skull. As the size of vessels and velocity of blood flow is not expected to differ on average between the two imaging conditions, the apparent increase in vessel diameter imaged through the skull versus WttB implant is likely due to the blurring of the image through the skull. In general, the light transmission to the brain and reflection from the brain are lower in the through-skull image. Additionally, the skull scattering disorders the speckle pattern that was created by the brain hemodynamics. The skull poses these same issues for the MSRI imaging as well, and because the skull texture is not homogeneous, image correction or enhancement is very complex [61]. The reduction in border sharpness of the vessels imaged through the skull versus WttB implant is consistent with this explanation, and the blurred nature of the through-skull image compared with the through-implant image is visually apparent in Figure 3b. It should also be noted that while the SNR and sharpness of the through-implant images are an improvement over the through-skull images, the mouse skull is inherently transparent itself [61], which is not the case in larger animals or humans.

While vein-artery separation is possible by MSRI alone, in this study we combine MSRI with LSI. The combination with LSI has two major benefits. First, some of the microvessels are not visible through the WttB implant by MSRI since the transmitted light could not overcome the reflected light from the surface of the implant for these visible wavelengths (560–610 nm), and the microvessels have low contrast when compared with larger vessels. Registering the information from the MSRI to the LSI flow map, which does show the microvessels, helped to extend the arteriovenous information to the smaller vessel sizes, which were not visible by MSRI. Second, LSI imaging contains functional information (relative blood velocity), so combining these methods produces vasculature maps, which show relative velocities of flow within the separated arteries and veins. Figure 8 contains an example of how this method can produce arteriovenous vasculature network images weighted by relative blood flow velocity.

As seen in Figure 3b, much more precise velocity information, particularly of microvessels, can be detected through the WttB implant, while the reduced sharpness of the vessels imaged through skull obscures precise flow determinations (Figs. 3b and 7). Imaging microvessels (usually involving small arteries of less than 150 μm in diameter, arterioles, capillaries, and venules [1,2]) is important for many applications, as microcirculation plays a critical role in physiological processes such as tissue oxygenation and nutritional exchange [3]. Monitoring the spatiotemporal characteristics of microcirculation is crucial for studying the normal and pathophysiologic conditions of tissue metabolism. It is also useful for assessing microcirculatory dysfunction due to disease conditions such as type 2 diabetes, peripheral vascular disease, atherosclerotic coronary artery disease, obesity, heart failure, Alzheimer's, schizophrenia, and hypertension, among others [84–86]. In addition, quantification of dynamic blood flow, angiogenesis, and vessel density are critical for monitoring the progression of wound healing [87]. Although high-resolution vascular network mapping is possible using imaging modalities such as CT, these approaches require injection of contrast agents and pose disadvantages such as radiation exposure. Existing noninvasive methodologies (including LSI through skull) are inadequate to study blood flow at microvessel resolution [88]. Windows such as the WttB implant are thus important tools for research, and in the case of the WttB implant can become important enablers of clinical diagnostics and therapy involving cerebral microvessels.

Creating novel windows for brain studies has been gaining attention recently [50,89–91]. Some of these studies, involving optical clearing agents (OCAs) applied to the scalp overlying native skull, have shown limited success due to optical losses and scattering in the skull [46]. These skin optical clearing strategies could work in conjunction with the WttB implant, to allow for imaging of cerebral blood flow in awake and behaving animals through closed scalp and implant, for example, to study cerebrovascular hemodynamic responses and tissue oxygenation to other stimuli.

Future studies by our group will explore this combined OCA-WttB strategy, as well as include additional imaging modalities that can couple with LSI to provide additive information, such as OCT and IOS.

There are several limitations to the current study. The sample sizes used were small ($n = 1$), and further experiments are needed to confirm the reproducibility of these findings. While a permanent cranial implant can allow for less invasive imaging of the brain at later time points, it requires an initial implantation surgery, which carries associated risks such as infection.

## CONCLUSION

In conclusion, this study has demonstrated the ability to perform MSRI-LSI across a transparent cranial implant, to allow for cerebral vessel networks to be mapped, including microvessels. These images contain additional information such as vein-artery separation and relative blood flow velocities, information which is of value scientifically and medically. The WttB implant provides substantial improvements over imaging through the murine cranial bone, where microvessels are not visible and MSRI cannot be performed.

## ACKNOWLEDGMENTS

This study was supported by National Science Foundation (NSF-PIRE #1545852) and "Beca Mixta" from National Council of Science and Technology of Mexico (CONACYT) (741249). The authors would like to acknowledge Gottlieb Uahengo for fabricating the YSZ samples.

## REFERENCES

1. Raichle ME. Behind the scenes of functional brain imaging: a historical and physiological perspective. Proc Natl Acad Sci USA 1998;95(3):765–772.
2. Raichle ME. The neural correlates of consciousness: an analysis of cognitive skill learning. Philos Trans R Soc Lond B Biol Sci 353(1377):1889–1901.
3. Schwartz WJ, Smith CB, Davidsen L, et al. Metabolic mapping of functional activity in the hypothalamo-neurohypophysial system of the rat. Science 1979;205(4407):723–725.
4. Ghaffari H, Grant SC, Petzold LR, Harrington MG. Regulation of cerebrospinal fluid and brain tissue sodium levels by choroid plexus and brain capillary endothelial cell Na+, K+-ATPases during migraine. bioRxiv 2019. 572727. https://doi.org/10.1101/572727.
5. Gusnard DA, Raichle ME, Raichle ME. Searching for a baseline: functional imaging and the resting human brain. Nat Rev Neurosci 2001;2(10):685–694.
6. Hyder F, Kida I, Behar KL, Kennan RP, Maciejewski PK, Rothman DL. Quantitative functional imaging of the brain: towards mapping neuronal activity by BOLD fMRI. NMR Biomed 2001;14(7-8):413–431.
7. Ganesh T, Estrada M, Yeger H, Duffin J, Cheng H-LM. A non-invasive magnetic resonance imaging approach for assessment of real-time microcirculation dynamics. Sci Rep 2017;7(1):25–31.
8. Kidwell CS, Hsia AW. Imaging of the brain and cerebral vasculature in patients with suspected stroke: advantages and disadvantages of CT and MRI. Curr Neurol Neurosci Rep 2006;6(1):9–16.
9. Holdsworth DW, Thornton MM. Micro-CT in small animal and specimen imaging. Trends Biotechnol 2002;20(8):S34–S39.
10. Miles KA. Perfusion imaging with computed tomography: Brain and beyond. Eur Radiol 2006;16(S7):M37–M43. https://doi.org/10.1007/s10406-006-0194-1
11. Zhou J. Intraoperative imaging of the brain macro- and microcirculation. Appl Cardiopulm Pathophysiol 2012;16:270–275.
12. Bash S, Villablanca JP, Jahan R, et al. Intracranial vascular stenosis and occlusive disease: Evaluation with CT angiography, MR angiography, and digital subtraction angiography. Am J Neuroradiol 2005;26(5):1012–1021.
13. Towle EL, Richards LM, Shams Kazmi SM, Fox DJ, Dunn AK. Comparison of indocyanine green angiography and laser speckle contrast imaging for the assessment of vasculature perfusion. Neurosurgery 2012;71(5):1023–1031. https://doi.org/10.1227/neu.0b013e31826adf88
14. Scerrati A, Della Pepa GM, Conforti G, et al. Indocyanine green video-angiography in neurosurgery: A glance beyond vascular applications. Clin Neurol Neurosurg 2014;124:106–113.
15. Jonathan E, Enfield J, Leahy MJ. Correlation mapping method for generating microcirculation morphology from optical coherence tomography (OCT) intensity images. J Biophotonics 2011;4(9):583–587.
16. Hu S, Maslov K, Tsytsarev V, Wang LV. Functional transcranial brain imaging by optical-resolution photoacoustic microscopy. J Biomed Opt 2009;14(4):040503.
17. Leahy MJ. Microcirculation Imaging. Hoboken, NJ: John Wiley & Sons; 2012.
18. Devor A, Sakadžić S, Srinivasan VJ, et al. Frontiers in optical imaging of cerebral blood flow and metabolism. J Cereb Blood Flow Metab 2012;32(7):1259–1276.
19. Tsytsarev V, Rao B, Maslov KI, Li L, Wang LV. Photoacoustic and optical coherence tomography of epilepsy with high temporal and spatial resolution and dual optical contrasts. J Neurosci Methods 2013;216(2):142–145.
20. Gottschalk S, Fehm TF, Deán-Ben XL, Tsytsarev V, Razansky D. Correlation between volumetric oxygenation responses and electrophysiology identifies deep thalamocortical activity during epileptic seizures. Neurophotonics 2017;4(1):011007.
21. Zhang Q, Lee CS, Chao J, et al. Wide-field optical coherence tomography based microangiography for retinal imaging. Sci Rep 2016;6:22017.
22. Sun J, Lindvere L, vanRaaij ME, Dorr A, Stefanovic B, Foster FS. In vivo imaging of cerebral hemodynamics using high-frequency micro-ultrasound. Cold Spring Harb Protoc 2010;2010(9):5495.
23. Alam SK, Kaisar Alam S, Parker KJ. Implementation issues in ultrasonic flow imaging. Ultrasound Med Biol 2003;29(4):517–528. https://doi.org/10.1016/s0301-562(02)00704-4
24. Klein KU, Stadie A, Fukui K, et al. Measurement of cortical microcirculation during intracranial aneurysm surgery by combined laser-Doppler flowmetry and photospectrometry. Neurosurgery 2011;69(2):391–398.
25. Zhao L, Li Y, Lu H, Yuan L, Tong S. Separation of cortical arteries and veins in optical neurovascular imaging. J Innov Opt Health Sci 2014;07(03):1350069.
26. Shi R, Chen M, Tuchin VV, Zhu D. Accessing to arteriovenous blood flow dynamics response using combined laser speckle contrast imaging and skin optical clearing. Biomed Opt Express 2015;6(6):1977–1989.
27. Ba AM, Guiou M, Pouratian N, et al. Multiwavelength optical intrinsic signal imaging of cortical spreading depression. J Neurophysiol 2002;88(5):2726–2735.
28. Dunn AK, Devor A, Bolay H, et al. Simultaneous imaging of total cerebral hemoglobin concentration, oxygenation, and blood flow during functional activation. Opt Lett 2003;28(1):28–30.
29. Lu G, Fei B. Medical hyperspectral imaging: A review. J Biomed Opt 2014;19(1):10901.
30. Torricelli A, Contini D, Pifferi A, et al. Time domain functional NIRS imaging for human brain mapping. NeuroImage 2014;85(Pt 1):28–50.
31. Jones PB, Shin HK, Boas DA, et al. Simultaneous multispectral reflectance imaging and laser speckle flowmetry of cerebral blood flow and oxygen metabolism in focal cerebral ischemia. J Biomed Opt 2008;13(4):044007.
32. Afromowitz MA, Callis JB, Heimbach DM, DeSoto LA, Norton MK. Multispectral imaging of burn wounds: A new clinical

instrument for evaluating burn depth. IEEE Trans Biomed Eng 1988;35(10):842–850. https://doi.org/10.1109/10.7291
33. Ferris DG, Lawhead RA, Dickman ED, et al. Multimodal hyperspectral imaging for the noninvasive diagnosis of cervical neoplasia. J Lower Genital Tract Dis 2001;5(2):65–72. https://doi.org/10.1097/00128360-200104000-00001
34. Benavides J, Chang S, Park S, et al. Multispectral digital colposcopy for in vivo detection of cervical cancer. Opt Express 2003;11(10):1223. https://doi.org/10.1364/oe.11.001223
35. Sakadžić S, Yuan S, Dilekoz E, et al. Simultaneous imaging of cerebral partial pressure of oxygen and blood flow during functional activation and cortical spreading depression. Appl Opt 2009;48(10):D169. https://doi.org/10.1364/ao.48.00d169
36. Shin HK, Dunn AK, Jones PB, et al. Normobaric hyperoxia improves cerebral blood flow and oxygenation, and inhibits peri-infarct depolarizations in experimental focal ischaemia. Brain 2007;130(6):1631–1642. https://doi.org/10.1093/brain/awm071
37. Shin HK, Nishimura M, Jones PB, et al. Mild induced hypertension improves blood flow and oxygen metabolism in transient focal cerebral ischemia. Stroke 2008;39(5):1548–1555. https://doi.org/10.1161/strokeaha.107.499483
38. Dunn AK, Devor A, Dale AM, Boas DA. Spatial extent of oxygen metabolism and hemodynamic changes during functional activation of the rat somatosensory cortex. NeuroImage 2005;27(2):279–290. https://doi.org/10.1016/j.neuroimage.2005.04.024
39. Drew PJ, Shih AY, Driscoll JD, et al. Chronic optical access through a polished and reinforced thinned skull. Nat Methods 2010;7(12):981–984. https://doi.org/10.1038/nmeth.1530
40. Hillman EMC. Optical brain imaging in vivo: Techniques and applications from animal to man. J Biomed Opt 2007;12(5):051402. https://doi.org/10.1117/1.2789693
41. Damestani Y, Reynolds CL, Szu J, et al. Transparent nanocrystalline yttria-stabilized-zirconia calvarium prosthesis. Nanomed Nanotechnol Biol Med 2013;9(8):1135–1138. https://doi.org/10.1016/j.nano.2013.08.002
42. Davoodzadeh N, Cano-Velázquez MS, Halaney DL, Jonak CR, Binder DK, Aguilar G. Evaluation of a transparent cranial implant as a permanent window for cerebral blood flow imaging. Biomed Opt Express 2018;9(10):4879. https://doi.org/10.1364/boe.9.004879
43. Davoodzadeh N, Aguilar G, Jonak C, et al. Laser speckle imaging of brain blood flow through a transparent nanocrystalline yttria-stabilized-zirconia cranial implant. Dyn Fluct Biomed Photonics 2018;10493:2. https://doi.org/10.1117/12.2285953.
44. Bouchard MB, Chen BR, Burgess SA, Hillman EMC. Ultrafast multispectral optical imaging of cortical oxygenation, blood flow, and intracellular calcium dynamics. Opt Express 2009;17(18):15670. https://doi.org/10.1364/oe.17.015670
45. Parthasarathy AB, Shams Kazmi SM, Dunn AK. Quantitative imaging of ischemic stroke through thinned skull in mice with multi exposure speckle imaging. Biomed Opt Express 2010;1(1):246. https://doi.org/10.1364/boe.1.000246
46. Zhang C, Feng W, Zhao Y, et al. A large, switchable optical clearing skull window for cerebrovascular imaging. Theranostics 2018;8(10):2696–2708.
47. Zhao Y-J, Yu T-T, Zhang C, et al. Skull optical clearing window for in vivo imaging of the mouse cortex at synaptic resolution. Light Sci Appl 2018;7:17153–17153.
48. Wang J, Zhang Y, Xu TH, Luo QM, Zhu D. An innovative transparent cranial window based on skull optical clearing. Laser Phys Lett 2012;9(6):469–473. https://doi.org/10.7452/lapl.201210017
49. Chen BR, Bouchard MB, McCaslin AFH, Burgess SA, Hillman EMC. High-speed vascular dynamics of the hemodynamic response. NeuroImage 2011;54(2):1021–1030. https://doi.org/10.1016/j.neuroimage.2010.09.036
50. Heo C, Park H, Kim Y-T, et al. A soft, transparent, freely accessible cranial window for chronic imaging and electrophysiology. Sci Rep 2016;6(1) .
51. Smith SS, Magnusen P, Pletka BJ. Fracture toughness of glass using the indentation fracture technique. In: Freiman S, Fuller E, editors. Fracture Mechanics for Ceramics, Rocks, and Concrete. West Conshohocken, PA: ASTM International; 1981. pp 33–45.
52. Hulbert SF. The use of alumina and zirconia in surgical implants. Introd Bioceram 1993; 25–40.
53. Aguilar G, Davoodzadeh N, Halaney D, Uahengo G, Garay JE. Influence of low temperature ageing on optical and mechanical properties of transparent yittria stabilized-zirconia cranial prosthesis. Des Qual Biomed Technol 2018;10486:9. https://doi.org/10.1117/12.2287296.
54. Gutierrez MI, Penilla EH, Leija L, Vera A, Garay JE, Aguilar G. Novel cranial implants of yttria-stabilized zirconia as acoustic windows for ultrasonic brain therapy. Adv Healthc Mater 2017;6(21):1700214. https://doi.org/10.1002/adhm.201700214
55. Cano-Velázquez MS, Davoodzadeh N, Halaney D, et al. Evaluation of optical access to the brain in the near infrared range with a transparent cranial implant. Latin America Optics and Photonics Conference. 2018. doi:10.1364/laop.2018.tu5c.2
56. Davoodzadeh N, Cuando N, Aminfar AH, Cano M, Aguilar G. Assessment of Bacteria Growth Under Transparent Nanocrystalline Yttria Stabilized-Zirconia Cranial Implant Using Laser Speckle Imaging. Hoboken, NJ: Wiley; 2018;50:pp S5–S6.
57. Casolco SR, Xu J, Garay JE. Transparent/translucent polycrystalline nanostructured yttria stabilized zirconia with varying colors. Scr Mater 2008;58(6):516–519.
58. Park J. Bioceramics: Properties, Characterizations, and Applications. Berlin, Germany: Springer Science & Business Media; 2009.
59. Garay JE. Current-activated, pressure-assisted densification of materials. Ann Rev Mater Res 2010;40(1):445–468. https://doi.org/10.1146/annurev-matsci-070909-104433
60. Cheng H, Luo Q, Zeng S, Chen S, Cen J, Gong H. Modified laser speckle imaging method with improved spatial resolution. J Biomed Opt 2003;8(3):559. https://doi.org/10.1117/1.1578089
61. Li P, Ni S, Zhang L, Zeng S, Luo Q. Imaging cerebral blood flow through the intact rat skull with temporal laser speckle imaging. Opt Lett 2006;31(12):1824. https://doi.org/10.1364/ol.31.001824
62. Li N, Jia X, Murari K, Parlapalli R, Rege A, Thakor NV. High spatiotemporal resolution imaging of the neurovascular response to electrical stimulation of rat peripheral trigeminal nerve as revealed by in vivo temporal laser speckle contrast. J Neurosci Methods 2009;176(2):230–236. https://doi.org/10.1016/j.jneumeth.2008.07.013
63. Robles FE, Chowdhury S, Wax A. Assessing hemoglobin concentration using spectroscopic optical coherence tomography for feasibility of tissue diagnostics. Biomed Opt Express 2010;1(1):310. https://doi.org/10.1364/boe.1.000310
64. Zhu D, Wang J, Zhi Z, Wen X, Luo Q. Imaging dermal blood flow through the intact rat skin with an optical clearing method. J Biomed Opt 2010;15(2):026008. https://doi.org/10.1117/1.3369739
65. Chen W, Park K, Volkow ND, Pan Y, Du C. Cocaine-induced abnormal cerebral hemodynamic responses to forepaw stimulation assessed by integrated multi-wavelength spectroimaging and laser speckle contrast imaging. IEEE J Sel Top Quantum Electron 2016;22(4):146–153. https://doi.org/10.1109/jstqe.2015.2503319
66. Frangi AF, Niessen WJ, Vincken KL, Viergever MA. Multiscale vessel enhancement filtering. In: Wells WM, Colchester A, Delp S, editors. Medical Image Computing and Computer-Assisted Intervention—MICCAI'98. Berlin, Heidelberg: Springer; 1998. pp 130–137.
67. Yousefi S, Qin J, Zhi Z, Wang RK. Label-free optical lymphangiography: Development of an automatic segmentation method applied to optical coherence tomography to visualize lymphatic vessels using Hessian filters. J Biomed Opt 2013;18(8):086004. https://doi.org/10.1117/1.jbo.18.8.086004
68. Kroon DJ. Hessian based Frangi Vesselness filter. MATLAB Central File Exchange. http://www.mathworks.com/matlabcentral/fileexchange/24409-hessian-based-frangivesselness-filter. Accessed Mar 02, 2010. 2009.
69. Fauver M, Seibel EJ, Richard Rahn J, et al. Three-dimensional imaging of single isolated cell nuclei using

optical projection tomography. Opt Express 2005;13(11): 4210. https://doi.org/10.1364/opex.13.004210
70. Prahl S. Optical absorption of hemoglobin. http://omlc.ogi.edu/spectra/hemoglobin. 1999. Accessed Dec 17, 2018.
71. Gourley JK, Heistad DD. Characteristics of reactive hyperemia in the cerebral circulation. Am J Physiol Heart Circ Physiol 1984;246(1):H52–H58. https://doi.org/10.1152/ajpheart.1984.246.1.h52
72. Dufour S, Atchia Y, Gad R, Ringuette D, Sigal I, Levi O. Evaluation of laser speckle contrast imaging as an intrinsic method to monitor blood brain barrier integrity. Biomed Opt Express 2013;4(10):1856. https://doi.org/10.1364/boe.4.001856
73. Postnov DD, Erdener SE, Kilic K, Boas DA. Cardiac pulsatility mapping and vessel type identification using laser speckle contrast imaging. Biomed Opt Express 2018;9(12):6388. https://doi.org/10.1364/boe.9.006388
74. Wang Y, Hu D, Liu Y, Li M. Cerebral artery–vein separation using 0.1-Hz oscillation in dual-wavelength optical imaging. IEEE Trans Med Imaging 2011;30(12):2030–2043. https://doi.org/10.1109/tmi.2011.2160191
75. Narasimha-Iyer H, Beach JM, Khoobehi B, Roysam B. Automatic identification of retinal arteries and veins from dual-wavelength images using structural and functional features. IEEE Trans Biomed Eng 2007;54(8):1427–1435. https://doi.org/10.1109/tbme.2007.900804
76. Schiessl I, Wang W, McLoughlin N. Independent components of the haemodynamic response in intrinsic optical imaging. NeuroImage 2008;39(2):634–646. https://doi.org/10.1016/j.neuroimage.2007.09.022
77. Grinvald A, Hildesheim R, Vanzetta I. Compartment-resolved imaging of activity dependent dynamics of cortical blood volume and oximetry. J Cereb Blood Flow Metab 2005;25(1_suppl):S681–S681. https://doi.org/10.1038/sj.jcbfm.9591524.0681
78. Luo Z, Yuan Z, Pan Y, Du C. Simultaneous imaging of cortical hemodynamics and blood oxygenation change during cerebral ischemia using dual-wavelength laser speckle contrast imaging. Opt Lett 2009;34(9):1480. https://doi.org/10.1364/ol.34.001480
79. Zhang HF, Maslov K, Sivaramakrishnan M, Stoica G, Wang LV. Imaging of hemoglobin oxygen saturation variations in single vesselsin vivousing photoacoustic microscopy. Appl Phys Lett 2007;90(5):053901. https://doi.org/10.1063/1.2435697
80. Miao P, Li M, Li N, et al. Detecting cerebral arteries and veins: From large to small. J Innov Opt Health Sci 2010;03(01):61–67. https://doi.org/10.1142/s1793545810000794
81. Feng N, Qiu J, Li P, et al. Simultaneous automatic arteries-veins separation and cerebral blood flow imaging with single-wavelength laser speckle imaging. Opt Express 2011;19(17):15777. https://doi.org/10.1364/oe.19.015777
82. Hu D, Wang Y, Liu Y, Li M, Liu F. Separation of arteries and veins in the cerebral cortex using physiological oscillations by optical imaging of intrinsic signal. J Biomed Opt 2010;15(3):036025. https://doi.org/10.1117/1.3456371
83. MacKenzie LE, Harvey AR. Oximetry using multispectral imaging: Theory and application. J Opt 2018;20(6):063501. https://doi.org/10.1088/2040-8986/aab74c
84. Fowkes FGR, Rudan D, Rudan I, et al. Comparison of global estimates of prevalence and risk factors for peripheral artery disease in 2000 and 2010: A systematic review and analysis. Lancet 2013;382(9901):1329–1340. https://doi.org/10.1016/s0140-6736(13)61249-0
85. Sokolnicki LA, Roberts SK, Wilkins BW, Basu A, Charkoudian N. Contribution of nitric oxide to cutaneous microvascular dilation in individuals with type 2 diabetes mellitus. Am J Physiol Endocrinol Metab 2007;292(1):E314–E318. https://doi.org/10.1152/ajpendo.00365.2006
86. Khalil Z, LoGiudice D, Khodr B, Maruff P, Masters C. Impaired peripheral endothelial microvascular responsiveness in Alzheimer's disease. J Alzheimer's Dis 2007;11(1):25–32. https://doi.org/10.3233/jad-2007-11106
87. Gnyawali SC, Barki KG, Mathew-Steiner SS, et al. High-resolution harmonics ultrasound imaging for non-invasive characterization of wound healing in a pre-clinical swine model. PLoS One 2015;10(3):e0122327. https://doi.org/10.1371/journal.pone.0122327
88. Sturesson C, Nilsson J, Eriksson S. Non-invasive imaging of microcirculation: A technology review. Med Dev 2014;7:445–452. https://doi.org/10.2147/mder.s51426
89. Kisler K, Lazic D, Sweeney MD, et al. In vivo imaging and analysis of cerebrovascular hemodynamic responses and tissue oxygenation in the mouse brain. Nat Protoc 2018;13(6):1377–1402. https://doi.org/10.1038/nprot.2018.034
90. Holtmaat A, Bonhoeffer T, Chow DK, et al. Long-term, high-resolution imaging in the mouse neocortex through a chronic cranial window. Nat Protoc 2009;4(8):1128–1144. https://doi.org/10.1038/nprot.2009.89
91. Costantini I, Ghobril J-P, Di Giovanna AP, et al. A versatile clearing agent for multi-modal brain imaging. Sci Rep 2015;5(1).